Modeling the Optical Efficiency of AlGaN/GaN Light Emission Diodes with 2D Carrier Localization

Alexandra Ibanez, Wilfried Desrat, Guillaume Cassabois, Julien Brault, Bernard Gil

physica status solidi pss a
www.pss-a.com

Modeling the Optical Efficiency of AlGaN/GaN Light Emission Diodes with 2D Carrier Localization

Alexandra Ibanez, Wilfried Desrat, Guillaume Cassabois, Julien Brault, and Bernard Gil**

The efficiency of nitride-based optical devices, with particular focus on $Al_xGa_{1-x}N$/AlN quantum wells used for deep ultraviolet light emission is investigated. The study addresses the wavelength dependence of the photoluminescence and in particular the drop in efficiency as the emission wavelength decreases from 250 nm to 210 nm. A model is developed that incorporates the effects of hole state symmetry changes, built-in strain, quantum confinement, and 2D electron-hole localization. The latter is introduced as a Gaussian potential representing the spatial alloy disorder in the heterostructures. This model shows good agreement with experimental data and emphasizes that the localization mechanism is crucial for understanding the light emission behavior.

1. Introduction

Since the first report of light emission in a crystal subjected to an external voltage by Henry Round in 1907,[1] and the realization of the first "light-emitting diode" by Oleg Losev, as documented by Fred Schubert in his series of topical monographs,[2] tens of thousands of researchers have focused on the problem of producing efficient compact solid-state light emitters based on semiconductors. Significant progress has been made with the development of the quantum theory of the solid state over time, on the one hand, and with the understanding of the principles governing the interaction of the electronic states of a solid with the electromagnetic field, on the other. These, together with advances in various technological processes, gave rise to the modern electronics industry. Important steps were taken with the invention of the p–n junction, based on the use of various types of semiconductors and, later, their heterostructures. Most of the operating devices have been initially based on the III–V compounds, that are crystals formed with any metal elements of the III column of the Mendeleev table associated with group V elements such as P, As, Sb. Later, heterostructures were used to control the bandgap and thus produce light at desired wavelengths, either by spontaneous or stimulated emission of photons. Technologies alternative to this III–V route have not really been successful, with misfortunes linked to the intrinsic properties of the semiconductors (such as the indirect bandgap of Si and Ge), the poor structural quality of the crystalline stacks, or the lack of possibility to grow the materials under n- and p-type doping,[3] in other words, many drawbacks that engineers have not been able to overcome with a view to commercialization. Then, for perhaps a quarter of a century, it was impossible to produce a blue light emitter or device with a wavelength shorter than the greenish one (use of nitrogen as isoelectronic dopant of GaP[2]), even using the most advanced epitaxial growth methods, despite the many efforts devoted to it worldwide.

Then in Japan, at the Meijo University of Nagoya, a breakthrough was made in the group of Isamu Akasaki, as reported by Y. Nanishi,[4] which paved the way for the exploration of "the blue Eldorado." This led to the study of the group III-element nitride semiconductors, which could be obtained in both n- and p-type device qualities, and quickly offered the possibility of growing and selling devices operating from the green to violet parts of the light spectrum. Ammonia or dinitrogen were then used as nitrogen precursors in growth reactors designed to operate at higher temperatures than for the other III–V compounds. Although the concepts for the designs of these light emitters have been rapidly framed, thanks to the previous work dedicated to the arsenides and antimonides,[4–7] the mechanisms that make it possible to explain the efficiency of the light emission, to optimize the electrical injection, and/or the extraction of the light are still to be definitively established, although many advances have been made with regard to the blue light emitters.[6–12]

Much work remains to be done, for example, to understand how to produce orange and red light emitters using nitrides and how to grow and fabricate them to challenge the arsenides and phosphides with a more environmentally friendly technology. At the other end of the visible spectrum, in the ultraviolet range, the solution currently being explored is to combine carrier

A. Ibanez, W. Desrat, G. Cassabois, B. Gil
Laboratoire Charles Coulomb (L2C)
Université de Montpellier, CNRS
FR-34095 Montpellier, France
E-mail: wilfried.desrat@umontpellier.fr; bernard.gil@umontpellier.fr

J. Brault
CNRS, CRHEA
Université Côte d'Azur
Rue Bernard Gregory, F-06560 Valbonne, France

The ORCID identification number(s) for the author(s) of this article can be found under https://doi.org/10.1002/pssa.202500284.

DOI: 10.1002/pssa.202500284

confinement wells based on $Al_xGa_{1-x}N$ alloys with AlN or $Al_yGa_{1-y}N$ barrier layers with $y > x$. The bandgap of GaN is ≈3.5 eV (350 nm) and that of AlN around 6 eV (205 nm). The bandgap of $Al_xGa_{1-x}N$ alloys lies in between. Then, by growing quantum wells (QWs) of different thicknesses, the whole spectrum can be covered down to 210 nm.[13] Indeed, we have reported light emission at 209 nm in QWs grown by molecular beam epitaxy (MBE) on sapphire.[13] However, if we look at the performance of light emission diodes, emitting light in the deep ultraviolet,[12,14] we see that the efficiency of the devices collapses when the light emission is reduced from 260 nm to 210 nm. This is interpreted qualitatively in samples grown worldwide, on the (0001) plane, in terms of the topmost valence band wavefunction switching from the (p_x, p_y)-type symmetry to the p_z-like one, which prevents the efficient extraction of TE-polarized light in favor of TM-polarized emission, as expected from the description of the valence band physics of these devices in terms of the translational invariant **k.p** theory. A rapid calculation of the wavefunction of the uppermost valence band among the triplets of p_x-like, p_y-like, and p_z-like states as a function of an equivalent crystal field parameter, by extending to strained $Al_yGa_{1-y}N$ what we have previously done for GaN,[15] does not seem fully convincing to explain accurately the evolution of the light emission efficiency over a wide range of wavelengths.

Based on this report, and also considering the still continuing active research on the InGaN related blue light emitters and the extreme difficulty to treat the influence of alloy disorder, defects and Auger recombination, an important nonradiative carrier recombination mechanism,[16] for the interpretation of the internal quantum efficiency in such samples,[11] we have chosen to focus on this problem for the ($Al_xGa_{1-x}N$)/AlN heterostructures. In this article, the localization effect is treated in terms of an original 2D potential that is spatially Gaussian in the growth plane, while the z-dependent envelope functions that account for the confinement of electrons and holes are computed in the traditional way, as the product of one-band envelope functions by the Bloch states of the valence band.[17] We show that the Gaussian potential provides an analytical expression for the localization energy and the efficiency of the light–matter interaction as a function of the interfacial disorder. Our model gives a fairly good agreement with the experimental wavelength dependence of the PL intensity in the 210–320 nm range.

2. Photoluminescence Intensity versus Emission Wavelength

In a previous work[18] we studied a series of $Al_xGa_{1-x}N$ quantum dots (QDs) grown by MBE on micrometer-thick AlN pseudosubstrates deposited on sapphire, grown with an aluminum composition ranging from 20% to 70% and 2 nm of average height. The decrease in the lattice mismatch between $Al_xGa_{1-x}N$ and AlN when increasing the aluminum composition prevented us from forming QDs with nominal Al content greater than about 70%.[18] To go further, we grew complementary 2 nm thin QWs to enrich the series of comparable samples over a larger aluminum composition, up to 90%,[13] which could emit light down to 209 nm. We were thus able to extend the measurements of the anisotropy of the light emission at the edge of the samples

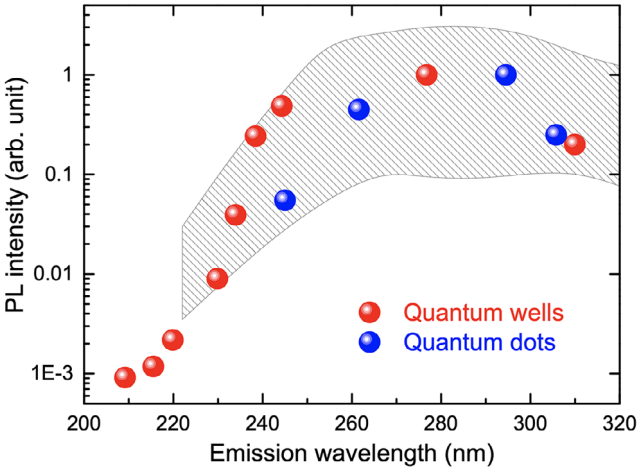

Figure 1. Experimental PL intensity as a function of the emission wavelength for $Al_xGa_{1-x}N$/AlN 2 nm-thick QWs and QDs (red and blue spheres).[13,18] The hatched area represents the data compiled by Kneissl.[12]

to a wider range of Al compositions, and we readily demonstrated the effect of alloy disorder on the shape of the emission diagram, on the Huang–Rhys factor, and on the broadening of the emission line. Our results are summarized in **Figure 1** as a function of the emission wavelength using red and blue spheres for QWs and QDs respectively. We observe a similar trend of the wavelength dependence of the photoluminescence (PL) intensity, which is arbitrarily set to unity for the maximum light emission at $x = 40\%$ Al composition, for both QDs and QWs. Our experimental results are in agreement with the overall literature data compiled by Kneissl et al.[12,14] and represented by the hatched area in Figure 1. We note that all our samples were grown by a single technique on similar AlN pseudotemplates. The layer thicknesses along the growth direction are identical and the barrier layers were aluminum nitride for all samples. The PL spectra were recorded using the same setup under identical temperature and excitation conditions.[13,18] All these conditions lead to a clear and solid trend of PL intensity versus emission wavelength, in contrast to the scattered data of Ref. [12,14] which are related to different experimental conditions such as heterostructure designs, setups, measured quantities, optical pump powers, etc. Our QW series data clearly show that the PL intensity decreases by almost three orders of magnitude as the wavelength decreases from 250 nm down to 210 nm, that is, for an aluminum composition increasing from 60% to 90% respectively. For wavelengths above 250 nm the PL intensity seems to saturate and even slightly fade for an aluminum composition of the order of 20% with an emission at 310 nm. This general behavior is also suggested by the hatched area in the background, reflecting the data collection by Kneissl.

3. Model

3.1. Valence Band Bloch States

To quantitatively disentangle the different physical contributions we write the wavefunction of the electron–hole pair recombining radiatively as follows

$$\Psi(\rho, z_e, z_h) = \psi_{eh}(\vec{\rho})\chi_e(z_e)\chi_h(z_h)u_c(\vec{r}_e)\sum_1^3 u_{v_i}(\vec{r}_h) \quad (1)$$

$\Psi(\rho)$ and ρ respectively represent the wavefunction and the in-plane position of the localized interacting electron–hole pair. The single $u_c(\vec{r}_e)$ and the three $u_{v_i}(\vec{r}_h)$ are the conduction and valence band Bloch waves at the center of the zone respectively. The spin degeneracy does not need to be represented in the above equation, although we represent the different valence band Bloch states in terms of the double group C_{6v} representations (Γ_9, Γ_7 and Γ_7'). These are the wavefunctions of a p electron with a spin in a uniaxial environment.[19] The spin–orbit interaction is included and mixes the eigenfunctions of the two Γ_7 and Γ_7' representations. The relative contributions of these three states are obtained using the **k.p** approach. The energies of the confined valence band states (we restrict ourselves here to the first confined hole states) are obtained as the solution of the following matrix

$$\begin{pmatrix} \Delta_1(x) + \Delta_2 + E_{\Gamma_5} & 0 & 0 \\ 0 & \Delta_1(x) - \Delta_2 + E_{\Gamma_5} & \sqrt{2}\Delta_3 \\ 0 & \sqrt{2}\Delta_3 & E_{\Gamma_1} \end{pmatrix} \quad (2)$$

where the confined energies E_{Γ_5} and E_{Γ_1} are obtained from the spinless calculation of the confined valence band levels. For simplicity, the two components of the spin–orbit operator Δ_2 (in-plane) and Δ_3 (on-axis), usually introduced to represent the anisotropy in wurtzite crystals, are chosen with identical values, equal to 6 meV, in both $Al_xGa_{1-x}N$ and AlN. The quantity $\Delta_1(x)$ represents the valence band splitting, which depends on the aluminum composition x in the QW. The experimental values of $\Delta_1^0(GaN) = 10\,meV$[20–23] and $\Delta_1^0(AlN) = -220\,meV$[24–26] are quantities with different signs. The top of the GaN valence band is twofold and has Γ_5 symmetry, while the top of the AlN valence band is the singlet Bloch state with Γ_1 symmetry. A symmetry crossover occurs for an aluminum composition of about 10%,[27,28] which has important consequences for the external quantum efficiency. The strain effects due to lattice matching of the $Al_xGa_{1-x}N$ layer to AlN lead to the dependence $\Delta_1(x) = -0.22x + 0.01(1-x) + 0.12x(1-x)$.[29] This results in a shift of this crossover composition to a greater aluminum composition of about 60%.[18,30] Above this Al composition the valence band Bloch states transform with dominant $p_z\begin{pmatrix}\uparrow\\\downarrow\end{pmatrix}$-like and ancillary $p_{x,y}\begin{pmatrix}\downarrow\\\uparrow\end{pmatrix}$-like. Since we are interested in the intensity of the light emitted through the (0001) plane with TE polarization, the relevant quantity is the fraction $|\xi|$ of $p_{x,y}\begin{pmatrix}\downarrow\\\uparrow\end{pmatrix}$-like states in the top valence band wavefunction. Within this notation the fraction of $p_z\begin{pmatrix}\uparrow\\\downarrow\end{pmatrix}$ is $\sqrt{1-\xi^2}$. In the equation above $\chi_e(z_e)$ and $\chi_h(z_h)$ are the unitary normalized functions, solutions of the quantum confinement in the $Al_xGa_{1-x}N$/AlN QW.

3.2. Quantum Well Confinement

The interplay between the different values of $\Delta_1(x)$ and $\Delta_1^0(AlN)$ and the existence of a band offset of chemical origin allows to anticipate the valence band arrangements. The bandgap mismatch between the $Al_xGa_{1-x}N$ QW layer and the AlN barrier is a fitting parameter expressed as a conduction band offset, $V_e/(V_e + V_{\Gamma_5})$, where V_e and V_{Γ_5} are the depths of the electron- and hole-confining potentials. In the simulation, the conduction band offset is fixed at 60% in accordance with the common value.[11] The bandgap dependence of the $Al_xGa_{1-x}N$ alloy is assumed to be equal to $E_g(x) = 6.25x + 3.48(1-x) - 0.85x(1-x)$.[29] The confined levels are easily obtained as solutions to a simple 1D potential problem with an electric field F_w in the QW layer of thickness L_w and another one F_b in the barrier layers of total thickness L_b. As usual, we apply the Born-von Karman approximation and assume that the potential drop is L_wF_w in the well layer. The electric field in the barrier layers F_b is defined by $L_wF_w + L_bF_b = 0$ and has therefore the opposite sign to F_w.[31] In the simulation, the electric field due to spontaneous and piezoelectric polarizations is fitted to 5 MV cm^{-1} for GaN/AlN ($x = 0$) and canceled for $x = 1$. This value is lower than the reported 9 MV cm^{-1} electric field in 2 nm GaN/AlN QWs,[32] but is used here as a fitting parameter in a similar way to that described in another study.[30] **Figure 2** shows that for a low-Al composition ($x = 0.5$) $Al_xGa_{1-x}N$ QW, the heavy hole (HH) and light hole (LH) valence bands are higher in energy than the split-off (CH) band, in contrast to what happens in the AlN barriers. Due to both a larger confinement potential and a heavier mass, taken to be equal to $2m_0$ for the HH/LH and 10 times lower ($0.2m_0$) for CH, where m_0 is the electron mass, the first confinement level of the HH/LH is above that of the CH. As the aluminum composition increases, the HH/LH and CH bands in the QW approach each other and, in the case of our simulation, become equal for $x = 0.63$. This corresponds to the intersection of the Γ_7 and Γ_7' levels in the inset of **Figure 3** when only the strain effect is considered. The confined levels are still not the same due to the different hole masses and barrier heights. For $x = 0.72$ the CH band is above the HH/LH bands in

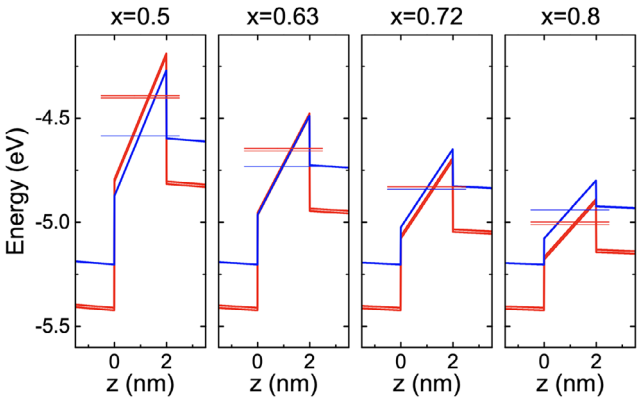

Figure 2. Heavy hole, light hole (red lines), and split-off valence bands (blue line) computed for a 2 nm-wide $Al_xGa_{1-x}N$/AlN QW, for four aluminum compositions: $x = 0.5$, 0.63, 0.72, and 0.8 from left to right. The thin horizontal lines are the first confined levels.

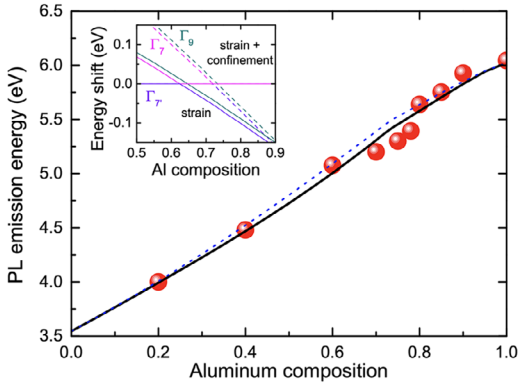

Figure 3. PL emission energy as a function of the aluminum composition of 2 nm $Al_xGa_{1-x}N$/AlN QWs. The dots are the experimental values and the lines are the computed energies of the optical transition between the confined conduction and valence levels with and without electron-hole 2D localization (solid and dotted lines). The relative energies of the Γ_i's valence band states with the strain only (solid lines) and strain and confinement (dashed lines) are drawn in the inset.

the well and in the barriers, but now the confining energies are the same. In other words, considering strain and confinement, the crossing of the Γ_7 and Γ_7' levels occurs at a higher Al composition of $x = 0.72$ for our 2 nm $Al_xGa_{1-x}N$/AlN QWs (see inset of Figure 3). For even higher aluminum contents the ground hole level is of CH nature (p_z state). The energies of the optical transitions between the ground electron state and the HH and CH levels are plotted in Figure 3 (dashed lines). This simulation result is in good agreement with the experimental PL emission energy (red spheres) measured for each x, validating the $Al_xGa_{1-x}N$ bandgap and electric field dependences versus x and the band offset values used.

3.3. Electron–Hole 2D Localization

In Equation (1), $\psi_{eh}(\vec{\rho})$ is a 2D envelope function representing the localization of the electron and hole in spatial fluctuations of the alloy potential. We approximate the localization in terms of a 2D circular potential of the Gaussian type

$$V(\rho) = V_0 e^{-\rho^2/\rho_0^2} = V_0 e^{-\alpha_0 \rho^2} \tag{3}$$

where the depth of the localization potential is defined by a positive V_0 in this notation and ρ_0 represents its in-plane extension. The 2D Schrödinger equation writes in terms of the in-plane mass of the particle under study, m_ρ

$$\left[\frac{\partial^2}{\partial\rho^2} + \frac{1}{\rho}\frac{\partial}{\partial\rho} + \frac{1}{\rho^2}\frac{\partial^2}{\partial\rho^2} + \frac{2m_\rho}{\hbar^2}(V(\rho) - E)\right]\psi_{eh}(\rho,\varphi) = 0 \tag{4}$$

Writing the unitary 2D normalized function $\psi_{eh}(\rho,\varphi) = R(\rho)\Theta(\varphi)$, we get two equations. The first one is

$$\frac{\partial^2}{\partial\varphi^2}\Theta(\varphi) = E\Theta(\varphi) \tag{5}$$

which eigenvectors are $\exp(\pm ik\varphi)$ and eigenvalues are k^2 with $k = 0, 1, 2, 3, \ldots$. Except for $k = 0$ the eigenvectors are twofold degenerate. Then we are left with the solution of an equation of the type

$$\left[\frac{\partial^2}{\partial\rho^2} + \frac{1}{\rho}\frac{\partial}{\partial\rho} - \frac{k^2}{\rho^2} + \frac{2m_\rho}{\hbar^2}(V(\rho) - E)\right]R(\rho) = 0 \tag{6}$$

We restrict our study to the ground state ($k = 0$) in a variational approach. The trial wavefunction is of the type $|\psi_\alpha\rangle = \sqrt{\frac{2\alpha}{\pi}}e^{(-\alpha\rho^2)}$ where α is a variational parameter. From this model we expect the oscillator strength $\|\psi_\alpha(0)\|^2$ to vary linearly with α.

The Schrödinger equation can be written as

$$-\frac{\hbar^2}{2m_\rho}(-4\alpha + 4\alpha^2\langle\psi_\alpha|\rho^2|\psi_\alpha\rangle) - V_0\langle\psi_\alpha|e^{-\alpha_0\rho^2}|\psi_\alpha\rangle - \langle\psi_\alpha|E|\psi_\alpha\rangle = 0 \tag{7}$$

Once calculated, the energy E is expressed as

$$E = \frac{\alpha\hbar^2}{m_\rho} - V_0\frac{2\alpha}{2\alpha + \alpha_0} \tag{8}$$

The minimization of $E(\alpha)$ leads to the value of α, the analytical solution of the ground state value of this 2D Gaussian well problem

$$\alpha = \frac{1}{2\rho_0^2}\left(\sqrt{\frac{2m_\rho V_0\rho_0^2}{\hbar^2}} - 1\right) \tag{9}$$

First, we notice that a threshold for localization in the 2D gaussian potential is reached when $2m_\rho\rho_0^2V_0/\hbar^2 > 1$. Second, the localization energy passes through a maximum at $|E_{max}| = V_0/4$ where the corresponding value of α_0 also reached a maximum equal to $\alpha_{0max} = m_\rho V_0/2\hbar^2$. Thus the 2D Gaussian localization problem is fully analytic and leads to the simple result that the oscillator strength is proportional to the localization potential. In the following we treat this potential in the framework of the disorder potential due to spatial fluctuations in semiconductor alloys developed by Baranovskii.[33,34] The energy scale depends on the material parameters as

$$\varepsilon_0 = \lambda\frac{\alpha^4x^2(1-x)^2m_\rho^3}{\hbar^6N^2} \tag{10}$$

In this equation, $\alpha = |dE_g/dx|$, where x is the aluminum composition of the $Al_xGa_{1-x}N$ QW, m_ρ is the effective mass of the e–h pair, and $N = 4/a^2c\sqrt{3}$ is the density of atomic sites in an hexagonal lattice of dimensions (a, c). The numerical factor λ is estimated to be $\approx 1/178$.[33,34] The localization term is plotted in **Figure 4** and peaks slightly above $x = 0.6$, instead of the expected half-alloy composition imposed by the $x^2(1-x)^2$ part, due to the bowing of the bandgap dependence versus x used in the model ($b = -0.85$). As described earlier, this results in a maximum confinement energy, which shifts the PL emission energy downward, as shown by the thick solid line in Figure 3.

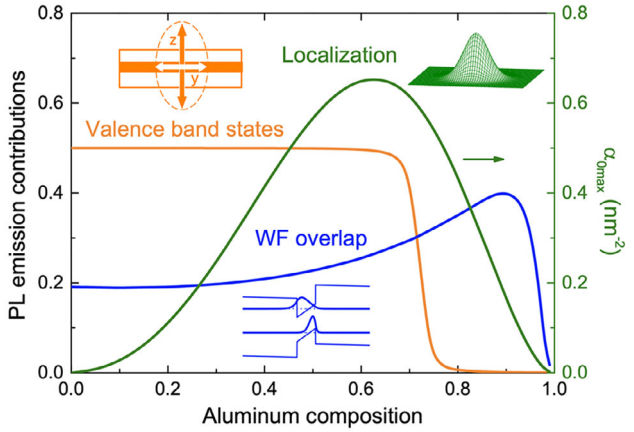

Figure 4. Physical contributions to the PL emission as a function of the aluminum composition of an $Al_xGa_{1-x}N$/AlN QW: valence band states within the **k.p** theory (orange), overlap of the electron and hole wavefunctions (blue), and electron–hole 2D localization (green). The latter is plotted in units of nm^{-2} on the right axis.

3.4. Oscillator Strength versus Emission Wavelength

Finally the oscillator strength for the emission process is proportional to the product of three terms

$$|\Psi(\vec{0})|^2 \propto |u_c(\vec{r}_e) I H_y I u_{v_i}(\vec{r}_h)|^2 \times |\psi_{eh}(\vec{0})|^2 \times \left|\int \chi_e(z)\chi_h(z)dz\right|^2 = |\xi| \times \alpha_{0max} \times \left|\int \chi_e(z)\chi_h(z)dz\right|^2 \quad (11)$$

where the first term $\langle u_c(\vec{r}_e)|H_y|u_{v_i}(\vec{r}_h)\rangle$ represents the dipolar interaction between the conduction band and the p-type valence band, previously called $|\xi|$. The second term is the electron–hole 2D localization due to spatial disorder, which is taken equal to α_{0max}. The last contribution is the matrix element of the envelope functions equal to the squared spatial overlap of the electron and hole wavefunctions of the confined states in the QW. These three contributions are plotted in Figure 4 as a function of the aluminum composition of the $Al_xGa_{1-x}N$ alloy. It is interesting to note the very different behavior of each mechanism. As already discussed, the change in the p-type states leads to an abrupt drop of the PL response to zero around $x = 0.7$, accompanied by a modification of its polarization. Outside this crossover region this contribution is independent of x. The localization term due to alloy disorder is 0 for $x = 0$ and 1 and is maximum for $x \approx 0.6$, which means that from $x = 0.6$ to 0.9, corresponding to wavelengths between 250 and 210 nm, electron–hole localization reduces the PL intensity. Finally, from $x = 0$ to 0.9, the overlap of the electron and hole wavefunctions slightly increases by a factor of 2. This is mainly related to the reduction of the electric field in the QW, widening the triangular confinement as shown in Figure 2, which is enhanced by the reduction of the barrier heights and the subsequent increase of the energy of the confined levels with increasing Al composition. Beyond $x = 0.9$ the overlap decreases due to a large spread of the wavefunction outside the well, but this high-Al composition range is not of interest in this study. In summary, at low x the PL emission is mainly limited by the negligible electron–hole localization due to weak alloy disorder. As the aluminum content increases, the latter becomes more significant and favors brighter emission until the upper valence band switches around 70%, extinguishing the light emission.

Figure 5 plots the experimental PL intensity of 2 nm-thick $Al_xGa_{1-x}N$/AlN QWs as a function of the emission wavelength with the simulated response curve. Obviously, the consideration of the three contributions, that is, the mixing of the valence band states with composition and strain, the quantum-confined Stark effect in all its manifestations, and finally the localization phenomenon, leads to a good description of the experimental data, both the PL emission energy versus x (Figure 3) and the PL intensity versus wavelength (Figure 5). It is evident that the localization term describes well the behavior from 320 to 250 nm and that the quenching of the $p_{x,y}$-like state below 240 nm accounts for the extinction of the PL intensity by three orders of magnitude. In this model the effects of the electric field and confinement seem to play a minor role, probably due to the reduced width (2 nm) of the studied QW. Indeed the overlap of the electron and hole wavefunctions, which ranges from 0.2 to 0.4 for x from 20% to 90%, is not the dominant contribution. Finally, our simple model shows that the consideration of the localization term, treated here in the case of a 2D Gaussian potential and in the framework of the alloy disorder theory, is important for the description of the light emission in nitride heterostructures. However, we cannot exclude the possibility that metallic atoms and topological defects such as dislocations also induce localized fluctuations in the potential that act as carrier localization centers, favoring radiative recombination.[35] It should be emphasized that a comprehensive multiband theory is still needed to improve the modeling of the physical data over the full wavelength range.

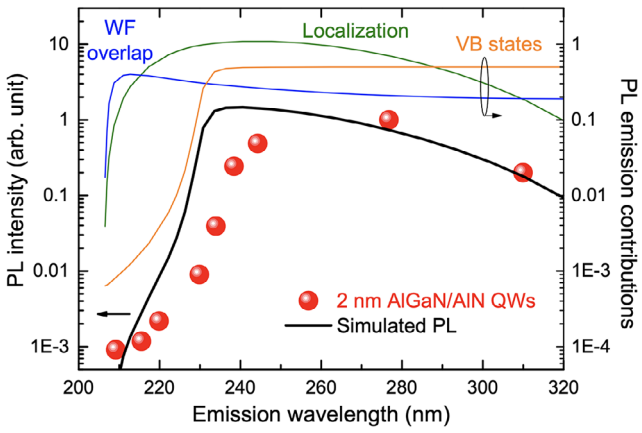

Figure 5. Experimental and simulated PL intensities as a function of the emission wavelength for 2 nm-wide $Al_xGa_{1-x}N$/AlN QWs, red spheres, and black solid line (left axis). The PL emission contributions (wavefunction (WF) overlap, electron–hole 2D localization, mixing of valence band (VB) states) are shown as thin solid lines (right axis).

4. Conclusion

We have reported an interpretation of the collapse of light emission efficiency by three decades between 250 and 209 nm in $Al_xGa_{1-x}N$/AlN QWs in the framework of a model that includes the variation of hole state symmetry with aluminum composition, built-in strain, and confinement effects. By further introducing alloy disorder, which induces interfacial localization of the interacting electron–hole pair, we were able to fit the slight increase of the PL emission intensity from 320 to 270 nm, which reaches a maximum in QWs with about 40% aluminum composition. We conclude that localization effects are a compelling contribution to the physics of light emission efficiency in $Al_xGa_{1-x}N$ heterostructures.

Acknowledgements

A.I. acknowledges the support of the French National Research Agency through the ANR project ANR-22-CE51-0035 "DOPALGAN" for the funding of her Ph.D. grant. The authors acknowledge the support by the French National Research Agency through ANR Project GANEX (ANR-11-LABX-0014). GANEX belongs to the publicly funded "Investissements d'Avenir" program managed by the French ANR agency.

Conflict of Interest

The authors declare no conflict of interest.

Data Availability Statement

The data that support the findings of this study are available from the corresponding author upon reasonable request.

Keywords

alloy disorder, aluminum nitride, deep ultraviolet emission, electron–hole localization, photoluminescence

Received: April 1, 2025
Revised: April 19, 2025
Published online:

[1] H. Round, *Electr. World* **1907**, *49*, 309.
[2] E. F. Schubert, *Light-Emitting Diodes*, Cambridge University Press, Cambridge, UK **2003**.
[3] A. Walsh, A. Zunger, *Nat. Mater.* **2017**, *16*, 964.
[4] Y. Nanishi, *Nat. Photonics* **2014**, *8*, 884.
[5] S. Nakamura, T. Mukai, M. Senoh, *Appl. Phys. Lett.* **1994**, *64*, 1687.
[6] S. Nakamura, M. Senoh, N. Iwasa, S.-I. N. Shin-ichi Nagahama, *Jpn. J. Appl. Phys.* **1995**, *34*, L797.
[7] T.-Y. Seong, J. Han, H. Amano, H. Morkoç, *Topics in Applied Physics*, Vol. *126*, Springer, Heidelberg, Germany **2013**.
[8] M. Filoche, M. Piccardo, Y.-R. Wu, C.-K. Li, C. Weisbuch, S. Mayboroda, *Phys. Rev. B* **2017**, *95*, 144204.
[9] A. David, *Phys. Rev. Appl.* **2021**, *15*, 054015.
[10] A. David, C. Weisbuch, *Phys. Rev. Res.* **2022**, *4*, 043004.
[11] T.-Y. Tsai, K. S. Qwah, J.-P. Banon, M. Filoche, C. Weisbuch, Y.-R. Wu, J. S. Speck, *Phys. Rev. Appl.* **2023**, *20*, 044069.
[12] M. Kneissl, T.-Y. Seong, J. Han, H. Amano, *Nat. Photonics* **2019**, *13*, 233.
[13] A. Ibanez, M. Leroux, N. Nikitskiy, W. Desrat, M. Moret, P. Valvin, G. Cassabois, J. Brault, B. Gil, F. Chugenji, K. Taiga, M. A. Khan, H. Hirayama, *Phys. Status Solidi B* **2024**, *261*, 2400215.
[14] M. Kneissl, J. Rass, *III-Nitride Ultraviolet Emitters*, Springer International Publishing, Cham **2016**.
[15] B. Gil, F. M. C. Hamdani, H. Morkoç, *Phys. Rev. B* **1996**, *54*, 7678.
[16] E. Kioupakis, D. Steiauf, P. Rinke, K. T. Delaney, C. G. Van de Walle, *Phys. Rev. B* **2015**, *92*, 035207.
[17] B. Gil, *Physics of Wurtzite Nitrides and Oxides*, Springer, Cham **2014**.
[18] A. Ibanez, N. Nikitskiy, A. Zaiter, P. Valvin, W. Desrat, T. Cohen, M. Ajmal Khan, G. Cassabois, H. Hirayama, P. Genevet, J. Brault, B. Gil, *J. Appl. Phys.* **2023**, *134*, 193103.
[19] D. L. Smith, C. Mailhiot, *Rev. Mod. Phys.* **1990**, *62*, 173.
[20] B. Gil, O. Briot, R.-L. Aulombard, *Phys. Rev. B* **1995**, *52*, R17028.
[21] S. Chichibu, A. Shikanai, T. Azuhata, T. Sota, A. Kuramata, K. Horino, S. Nakamura, *Appl. Phys. Lett.* **1996**, *68*, 3766.
[22] D. Volm, K. Oettinger, T. Streibl, D. Kovalev, M. Ben-Chorin, J. Diener, B. K. Meyer, J. Majewski, L. Eckey, A. Hoffmann, H. Amano, I. Akasaki, K. Hiramatsu, T. Detchprohm, *Phys. Rev. B* **1996**, *53*, 16543.
[23] R. Stepniewski, M. Potemski, A. Wysmołek, K. Pakuła, J. M. Baranowski, J. Łusakowski, I. Grzegory, S. Porowski, G. Martinez, P. Wyder, *Phys. Rev. B* **1999**, *60*, 4438.
[24] E. Silveira, J. A. Freitas, O. J. Glembocki, G. A. Slack, L. J. Schowalter, *Phys. Rev. B* **2005**, *71*, 041201.
[25] G. Rossbach, M. Feneberg, M. Röppischer, C. Werner, N. Esser, C. Cobet, T. Meisch, K. Thonke, A. Dadgar, J. Bläsing, A. Krost, R. Goldhahn, *Phys. Rev. B* **2011**, *83*, 195202.
[26] M. Feneberg, M. F. Romero, M. Röppischer, C. Cobet, N. Esser, B. Neuschl, K. Thonke, M. Bickermann, R. Goldhahn, *Phys. Rev. B* **2013**, *87*, 235209.
[27] M. Leroux, S. Dalmasso, F. Natali, S. Helin, C. Touzi, S. Laügt, M. Passerel, F. Omnes, F. Semond, J. Massies, P. Gibart, *Phys. Status Solidi B* **2002**, *234*, 887.
[28] K. B. Nam, J. Li, M. L. Nakarmi, J. Y. Lin, H. X. Jiang, *Appl. Phys. Lett.* **2004**, *84*, 5264.
[29] B. Neuschl, J. Helbing, M. Knab, H. Lauer, M. Madel, K. Thonke, T. Meisch, K. Forghani, F. Scholz, M. Feneberg, *J. Appl. Phys.* **2014**, *116*, 113506.
[30] R. G. Banal, M. Funato, Y. Kawakami, *Phys. Rev. B* **2009**, *79*, 121308.
[31] F. Bernardini, V. Fiorentini, D. Vanderbilt, *Phys. Rev. B* **1997**, *56*, R10024.
[32] C. Adelmann, E. Sarigiannidou, D. Jalabert, Y. Hori, J.-L. Rouvière, B. Daudin, S. Fanget, C. Bru-Chevallier, T. Shibata, M. Tanaka, *Appl. Phys. Lett.* **2003**, *82*, 4154.
[33] S. D. Baranovskii, A. Efros, *Sov. Phys. Semicond.* **1978**, *12*, 1328.
[34] S. D. Baranovskii, A. V. Nenashev, D. Hertel, F. Gebhard, K. Meerholz, *ACS Omega* **2022**, *7*, 45741.
[35] M. Funato, R. G. Banal, Y. Kawakami, *AIP Adv.* **2015**, *5*, 117115.